# Hierarchical carbon nanocages as high-rate anodes for Li- and Na-ion batteries

Zhiyang Lyu, Lijun Yang, Dan Xu, Jin Zhao, Hongwei Lai, Yufei Jiang, Qiang Wu, Yi Li, Xizhang Wang (✉), and Zheng Hu (✉)

## Just Accepted

**Hierarchical carbon nanocages as high-rate anodes for Li- and Na-ion batteries**

Zhiyang Lyu, Lijun Yang, Dan Xu, Jin Zhao, Hongwei Lai, Yufei Jiang, Qiang Wu, Yi Li, Xizhang Wang*, and Zheng Hu*

Nanjing University, China

Hierarchical carbon nanocages
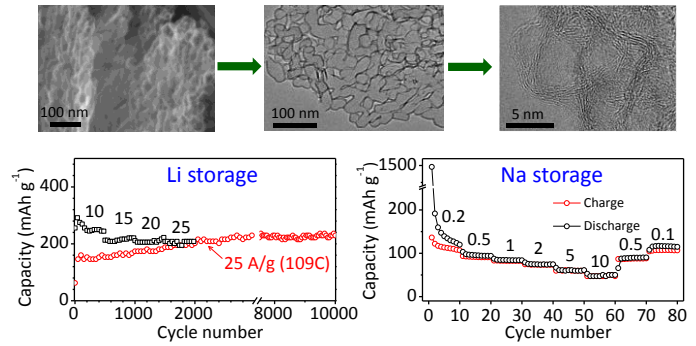


The unique structure of hierarchical carbon nanocages greatly favors the electrolyte penetration, ion diffusion, electron conduction and structural stability, resulting in high-rate capability and excellent cyclability for Li and Na storages.

# Hierarchical carbon nanocages as high-rate anodes for Li- and Na-ion batteries

Zhiyang Lyu, Lijun Yang, Dan Xu, Jin Zhao, Hongwei Lai, Yufei Jiang, Qiang Wu, Yi Li, Xizhang Wang (✉), and Zheng Hu (✉)

*Key Laboratory of Mesoscopic Chemistry of MOE, School of Chemistry and Chemical Engineering, Nanjing University, Nanjing, 210093, China.*

## ABSTRACT

The novel hierarchical carbon nanocages (hCNC) are first proposed as high-rate anodes for Li- and Na-ion batteries. The unique structure of porous network for hCNC greatly favors the electrolyte penetration, ion diffusion, electron conduction and structural stability, resulting in high-rate capability and excellent cyclability. For lithium storage, the corresponding electrode stores the steady reversible capacity of 970 mAh $g^{-1}$ at a rate of 0.1 A $g^{-1}$ after 10 cycles, and stabilizes at 229 mAh $g^{-1}$ even over 10000 cycles at a high rate of 25 A $g^{-1}$ (33 s for full-charging) while delivering a large specific power of 37 kW $kg_{electrode}^{-1}$ and specific energy of 339 Wh $kg_{electrode}^{-1}$. For sodium storage, the hCNC reaches a high discharge capacity of ~50 mAh $g^{-1}$ even at a high rate of 10 A $g^{-1}$.

## 1    Introduction

Lithium-ion batteries (LIBs) have widely been applied in cell phones, laptop computers and digital cameras, which creates great change for today's modern life [1, 2]. Beyond the portable electronic devices, the markets for large-scale energy storage have rapidly emerged, including powering electric vehicles and leveling the grid fed by intermittent sources such as solar and wind energies [3-5]. These new demands are calling for a significant step-up in rate capability, energy density and cost-competitive for nowadays LIBs.

In the viewpoint of rate capability, the limitation mainly stems from the slow solid-state Li-ion diffusion both in the cathode and anode materials, which prevents the massive Li-ions releasing or storing rapidly. Progress in the high-rate cathodes of LIBs has reached the half-cell capacity up to 60 mAh $g^{-1}$ at an ultrahigh rate of 400C (nC denotes the rate at which a full charge or discharge takes 1/n hour) [6-10]. The exploration of matchable high-rate anode

counterparts has become a challenge to realize the dramatic performance improvement of the full cells with ultrafast charging/discharging capability. To reduce the cost of LIBs, the sodium-ion batteries (SIBs) is considered to be an alternative to LIBs due to the abundance and low cost of sodium [10, 11]. And considerable progresses have been made in developing the cathode materials for SIBs to date [12-15]. Compared to the fast development of excellent cathode materials, the innovation of matchable anode materials for SIBs is relatively slow. Exploring the anodes featured with high capacity, high-rate capability, low cost and long cyclability is also a great challenge for SIBs.

The carbonaceous materials have been used as anodes in the commercial LIBs owing to the low cost, good conductivity and environmental benignity. The abundant carbon nanostructures give us opportunity to achieve the high surface area for electrolyte penetration and the short solid-state ion diffusion length for rapid ion transport [16-20]. Moreover, carbon nanomaterials avoid the bottlenecks of the large volume change during ions intercalation/deintercalation generally faced by the other typical anode materials, e.g. Si-based materials and metal oxides ($MO_x$) for Li storage [21] as well as Sn-based materials for Na storage [22, 23]. Therefore, carbon nanomaterials could be the most potential high-rate anodes for Li- and Na-ion batteries. In addition, constructing a 3D hierarchical architecture for carbon nanomaterials is also an effective approach to enhance ion diffusion, electron transportation and structural stability [24-26].

Very recently, we have obtained the novel 3D hierarchical carbon nanocages (hCNC) with well-defined multiscale characters and coexisting micro-, meso-, and macro-pores, which confines high-loading sulfur as high-rate Li-S batteries cathodes [27]. In this study, we first proposed the hCNC as Li- and Na-ion batteries anodes. The unique structure of hCNC greatly favors the electrolyte penetration, ion diffusion, electron conduction and structural stability, resulting in a high-rate capability and excellent cyclability.

## 2    Experimental

### 2.1   Preparation

The hierarchical carbon nanocages were prepared by an in-situ MgO template method using the basic magnesium carbonate precursor with 3D hierarchical structure, and the randomly packed carbon nanocages (rpCNC) was prepared similar to hCNC using the commercial MgO particles as the template, as described in our previous paper [27]. The preparation of carbon nanotubes (CNT) and reduced graphene oxides (RGO) were referenced from our previous papers [28, 29].

### 2.2   Characterization

The as-prepared materials were characterized by scanning electron microscopy (SEM, Hitachi S4800 at 20 kV), high resolution transmission electron microscopy (HRTEM, JEM-2100 operating at 200 kV). $N_2$ adsorption/desorption isotherms were measured on Thermo Fisher Scientific Surfer Gas Adsorption Porosimeter at 77 K. The specific surface area was calculated using the BET (Brunauer-Emmett-Teller) method based on the adsorption data. Micro- and meso-pore size distributions were calculated by using HK (Horvath-Kawazoe, $N_2$ on graphite at 77.2 K) and BJH (Barrett-Joyner-Halenda) methods from the adsorption branch of $N_2$ isotherm, respectively. Thermogravimetry analysis (Netzsch STA-449F3) was performed at a heating rate of 10 °C $min^{-1}$ from room temperature to 900 °C under air flow.

### 2.3   Electrochemistry

The working electrodes were prepared by casting the slurry containing the active materials (80 wt%) and polyvinylidene fluoride binder (PVDF, 20 wt%) in N-methyl-2-pyrrolidnone onto a Cu foil substrate. After dried in a vacuum oven at 120 °C for 12 h, the electrode was obtained with the thickness of 25~55 μm. No conducting carbon was used and the mass loading of active materials was 0.25~0.50 mg $cm^{-2}$. 2032 stainless-steel coin cells were assembled in an Ar-filled glovebox with both oxygen and humidity individually below 0.1 ppm. The Li-ion cells were assembled with Li metal foil as counter electrode, 1.0 mol $L^{-1}$ $LiPF_6$ in a solution of 1:1 (v/v) ethylene carbonate (EC) and dimethyl carbonate (DMC) as the electrolyte, and Celgard 2500 as the separator. The Na-ion cells were fabricated using Na metal foil as

anode, and 1.0 mol L$^{-1}$ NaClO$_4$ salt in propylene carbonate (PC) as the electrolyte. The charge-discharge performances of the half-cells were evaluated by NEWARE CT3008 multichannel battery testing unit in different constant current densities. The rate nC was calculated by the charge time (1/n hour) of the last cycle. The specific energy *E* and specific power *P* in a constant current charge/discharge process are calculated by the following equation

$$E = \int_0^t \frac{IV}{m} \mathrm{d}t \, , \quad P = \frac{1}{t}\int_0^t \frac{IV}{m} \mathrm{d}t$$

where *I*, *V*, *m*, and *t* are the current, voltage, mass of active material, and charging time, respectively [30].

## 3  Results and discussion

### 3.1  Characterizations

The hCNC was prepared by an in-situ MgO template method followed by the removal of the MgO template, as reported in our previous study [27]. Figure 1 shows the characterizations of the hCNC. The typical scanning electron microscopy (SEM) and transmission electron microscopy (TEM) images present the interconnected hollow carbon nanocages with a 3D hierarchical architecture (Figs. 1(a)-1(c)). The hollow nanocages have ca. 10~50 nm in size and 4~7 well-graphitized layers in thickness. The nitrogen adsorption/desorption isotherms demonstrate the hCNC owns the large specific surface area of 1051 m$^2$ g$^{-1}$ and the coexisting micro-, meso-, and macro-pores with a high micro-meso pore volume of 4.059 cm$^3$ g$^{-1}$ (Figs. 1(d) and 1(e)). The open system integrated the well-defined micro-meso-macro pore size distribution for hCNC favors the accessibility to electrolyte and the rapid solid-state ion diffusion. The unique hierarchical character of hCNC is much different from the case of the randomly packed carbon nanocages (rpCNC) (Fig. S1 in the Electronic Supplementary Material (ESM)) [27].

### 3.2  Lithium storage performance

The lithium storage performance of the hCNC is evaluated as presented in Fig. 2, by fabricating coin cells (2032) with a metallic Li counter electrode. The hCNC exhibits a high initial charge capacity of 1021

mAh g$^{-1}$ at a low current density of 0.1 A g$^{-1}$, and reaches a large and steady reversible capacity of ca. 970 mAh g$^{-1}$ after 10 cycles with a high Coulombic efficiency of ca. 95% (Figs. 2(a) and 2(b)), which is at high-level for carbon-based materials [26, 30-33]. The large plateau in the first discharge voltage profile in the range of 0.5~1.0 V originates from the formation of a solid electrolyte interphase (SEI) layer on the surfaces of the hCNC, which would lead to a high irreversible capacity but could be avoided by prelithiation (Fig. S2 in the ESM) [8, 34]. Even after various rates cycling, the steady reversible capacity of the hCNC still reaches the high value of ~190 mAh g$^{-1}$ at the high rate of 30 A g$^{-1}$, presenting an excellent reversibility and high-rate capability (Fig. 2(c) and Fig. S3 in the ESM). Moreover, the capacity fading of the hCNC is rather small at the high current density and the long-term cyclability is outstanding. The capacity stabilizes at 229 mAh g$^{-1}$ even over 10000 cycles at the high rate of 25 A g$^{-1}$ (Fig. 2(d) and Fig. S4 in the ESM), which derives from the excellent structural stability of the porous network that alleviates the stress and volume changes during the lithiation/delithiation. The structural advantage of the hCNC is also impressed by the higher reversible capacity and the better rate capability than those for the other morphological carbon nanostructures such as the rpCNC, CNT, and RGO (Fig. 3 and Figs S5-S7 in the ESM). In comparison with the cases for the other three typical carbon nanostructures, the much improved electrochemical performance of the hCNC suggests the great contribution of the unique 3D hierarchical architecture, which facilitates the penetration of electrolyte into the electrode, the solid-state Li-ion diffusion, and the electron conduction through the porous network.

The hCNC and rpCNC have similar units of carbon nanocages at the nanoscale, but quite different secondary structure at the mesoscale, i.e. the interconnected nanocages form the nanosheets with submicron-sized interspace for hCNC, while the nanocages are randomly packed for rpCNC (Fig. 1 and Fig. S1 in the ESM) [27]. This difference should be responsible for the much better rate performance of hCNC than rpCNC (Fig. 3). To understand the superiority of the 3D hierarchical architecture, we also performed the theoretical simulation by building a half-cell model with a 3D electrode as illustrated in

Fig. S8 in the ESM. Thus both experimental and theoretical results reveal the dramatic performance enhancement for the hCNC over the rpCNC arising from the well-defined multiscale characters of the former. The big improvement of properties is also observed for the organized CNT over the unorganized CNT [35]. Those results also demonstrate an effective exploration of advanced materials in the viewpoint of mesoscale science which is an exciting frontier attracting increasing attention [36, 37].

The Ragone plots for the hCNC, rpCNC, CNT, RGO and the state-of-the-art pure carbon materials based cells with lithium metal as the counter/reference electrode are shown in Fig. 4, which could be used to evaluate their application potentials. The specific energy and power was calculated based on the active mass of the carbon electrode. The plot of hCNC derived from Figs. 2(c) and 2(d) locates in the most upper-right side (Fig. 4a), i.e. the hCNC delivers the highest specific energy at the same specific power or vice versa. The stable performance of the hCNC reaches the high specific power of 37 kW kg$_{electrode}^{-1}$ comparable to supercapacitors [20] and specific energy of 339 Wh kg$_{electrode}^{-1}$ even after the long-term 10000 cycles under the high current density of 25 A g$^{-1}$ (109C, 33 s for full-charging), which presents the highest level for the state-of-the-art pure carbon anode materials of LIBs (Fig. S9) [38-41].

### 3.3 Sodium storage performance

The sodium storage performance of the hCNC is also evaluated by fabricating coin cells with a metallic Na counter electrode, as demonstrated in Fig. 5. At a low rate of 0.1 A g$^{-1}$, the hCNC reaches a large and steady discharge capacity of ~150 mAh g$^{-1}$ after 100 cycles with a high Coulombic efficiency of ca. 97% (Figs. 5(a) and 5(b)). The hCNC also exhibits a large initial irreversible capacity due to the formation of the SEI layer (Fig. 5(a)), which also could be avoided by presodiation [42]. As shown in Figs. 5(c) and 5(d), the hCNC presents a high-rate capability for sodium storage, delivering a high discharge capacity of ~50 mAh g$^{-1}$ even at a high rate of 10 A g$^{-1}$ after various rates cycling. The high-rate sodium storage performance of the hCNC is comparable to those of

other reported carbon-based nanomaterials, e.g. hollow carbon nanowires [43], hollow carbon nanospheres [44], carbon nanosheet frameworks [45], hierarchically porous carbon/graphene composite [46] and expanded graphite [47]. From Figure 5d, at very high current densities, e.g., 5 and 10 A g$^{-1}$, the charge-discharge curves have abnormal serrated characteristics, which can be ascribed to the very small specific capacities and the sparsely recordable data points as well.

The preceding results indicate that the hCNC is a new kind of high-rate anode material for Li- and Na-ion batteries, which results from the unique multiscale hierarchical architecture, as schematically shown in Fig. S10 in the ESM. The submicron-sized inter-sheet space of the porous hCNC with large specific surface area facilitates the penetration of electrolyte into the electrode. Moreover, the nano-sized dimensions of the cages and the abundant micropore tunnels of the unsealed shells insure the short solid-state ion diffusion length for rapid ion transport (Fig. S10(f) in the ESM). The micropore tunnels also allow the inner surface accessible for active ions, hence even more active sites are available (Fig. S11 in the ESM) [48]. Finally, the interconnection or sharing the carbon shells between the neighboring nanocages makes the hCNC keep a good conductivity for easy electron transportation [27].

As a new kind of carbon nanomaterials, the 3D hCNC can avoid the bottlenecks of the huge volume change during ions intercalation/deintercalation faced by the other typical anode materials [18-23], hence excellent cyclability and high-rate capability have been achieved. It is noted that the relatively low tap density of the hCNC is unfavorable, but its large specific capacity is favorable for the high volumetric energy density. As a result, at high current density the hCNC electrode stores higher volumetric capacity of Li storage than the commercial graphite powder electrode, which is expected for high-rate anode (Fig. S12 in the ESM). The large initial irreversible capacity is a common issue of nanomaterials for application in full batteries, which could be solved by prelithiation or presodiation [8, 34, 42].

To investigate the effect of the mass loading of electrodes on the rate performance, the electrodes with higher mass loading of 1.0~2.0 mg cm$^{-2}$ are

<mark>intentionally fabricated. With increasing the mass loading, the electrode films easily peeled off the substrates. The corresponding rate performance deteriorated, which could be attributed to the sluggish ion and electron transportations due to the thick and cracked films (Figure S13 in the ESM).</mark> Further efforts should be devoted to optimizing the pretreatments for large scale production and increasing the tap density of hCNC by developing some advanced processing [49, 50] <mark>or filling other anode materials into the hollow nanocages, such as silicon or metal oxides.</mark> Anyway, the novel multiscale hierarchical structure of the hCNC results in a high-rate capability and excellent cyclability for Li and Na storages.

## 4   Conclusions

The novel hierarchical carbon nanocages (hCNC) are first proposed as high-rate anodes for Li- and Na-ion batteries. For lithium storage, the corresponding electrode stores the steady reversible capacity of 970 mAh $g^{-1}$ at a rate of 0.1 A $g^{-1}$ after 10 cycles, and stabilizes at 229 mAh $g^{-1}$ even over 10000 cycles at a high rate of 25 A $g^{-1}$ while delivering a large specific power of 37 kW $kg_{electrode}^{-1}$ and specific energy of 339 Wh $kg_{electrode}^{-1}$. For sodium storage, the hCNC reaches a high discharge capacity of ~50 mAh $g^{-1}$ even at a high rate of 10 A $g^{-1}$. The high-rate capability and excellent cyclability results from the unique hierarchical structure which greatly favors the electrolyte penetration, solid-state ion diffusion, electron conduction and structural stability. Together with the facile, low-cost, and scalable fabrication process, this unique carbon nanomaterial provides a new candidate of anode materials for the high-rate LIBs and SIBs.

## Acknowledgements

**Electronic Supplementary Material**: Supplementary material (additional data) is available in the online version of this article at http://dx.doi.org/10.1007/s12274-***-****-* (automatically inserted by the publisher).

## References

[1]   Armand, M.; Tarascon, J. M. Building better batteries. *Nature* **2008**, *451*, 652-657.

[2]   Goodenough, J. B.; Park, K. S. The Li-ion rechargeable battery: a perspective. *J. Am. Chem. Soc.* **2013**, *135*, 1167-1176.

[3]   Dunn, B.; Kamath, H.; Tarascon, J. M. Electrical energy storage for the grid: a battery of choices. *Science* **2011**, *334*, 928-935.

[4]   Yang, Z.; Zhang, J.; Kintner-Meyer, M. C. W.; Lu, X.; Choi, D.; Lemmon, J. P.; Liu, J. Electrochemical energy storage for green grid. *Chem. Rev.* **2011**, *111*, 3577-3613.

[5]   Nazar, L. F.; Cuisinier, M.; Pang, Q. Lithium-sulfur batteries. *MRS Bull.* **2014**, *39*, 436-442.

[6]   Kang, B.; Ceder, G. Battery materials for ultrafast charging and discharging. *Nature* **2009**, *458*, 190-193.

[7]   Wang, H.; Yang, Y.; Liang, Y.; Cui, L. F.; Casalongue, H. S.; Li, Y.; Hong, G.; Cui, Y.; Dai, H. LiMn$_{(1-x)}$Fe$_{(x)}$PO$_{(4)}$ nanorods grown on graphene sheets for ultrahigh-rate-performance lithium ion batteries. *Angew. Chem. Int. Ed.* **2011**, *50*, 7364-7368.

[8]   Hassoun, J.; Lee, K. S.; Sun, Y. K.; Scrosati, B. An advanced lithium ion battery based on high performance electrode materials. *J. Am. Chem. Soc.* **2011**, *133*, 3139-3143.

[9]   Xiao, X.; Lu, J.; Li, Y. LiMn$_2$O$_4$ microspheres: synthesis, characterization and use as a cathode in lithium ion batteries. *Nano Res.* **2010**, *3*, 733-737.

[10]  Kim, S. W.; Seo, D. H.; Ma, H.; Ceder, G.; Kang, K. Electrode materials for rechargeable sodium-ion batteries: potential alternatives to current lithium-ion batteries. *Adv. Energy Mater.* **2012**, *2*,710-721.

[11]  Slater, M. D.; Kim, D.; Lee, E.; Johnson, C. S. Sodium-ion batteries. *Adv. Funct. Mater.* **2013**, *23*,947-958.

[12]  Yabuuchi, N.; Kajiyama, M.; Iwatate, J.; Nishikawa, H.; Hitomi, S.; Okuyama, R.; Usui, R.; Yamada, Y.; Komaba, S. P2-type Na$_x$[Fe$_{1/2}$Mn$_{1/2}$]O$_2$ made from earth-abundant elements for rechargeable Na batteries. *Nat. Mater.* **2012**, *11*, 512-517.

[13]  Wang, L.; Lu, Y.; Liu, J.; Xu, M.; Cheng, J.; Zhang, D.; Goodenough, J. B. A superior low-cost cathode for a Na-ion battery. *Angew. Chem. Int. Ed.* **2013**, *52*, 1964-1967.

[14]  You, Y.; Yu, X.; Yin, Y.; Nam, K. W.; Guo, Y. G. Sodium iron hexacyanoferrate with high Na content as a Na-rich cathode material for Na-ion batteries. *Nano Res.* in press, DOI: 10.1007/s12274-014-0588-7.

[15]  Wang, S.; Wang, L.; Zhu, Z.; Hu, Z.; Zhao, Q.; Chen, J. All organic sodium-ion batteries with Na$_4$C$_8$H$_2$O$_6$. *Angew. Chem.* **2014**, *126*, 6002-6006.

[16] Bruce, P. G.; Scrosati, B.; Tarascon, J. M. Nanomaterials for rechargeable lithium batteries. *Angew. Chem. Int. Ed.* **2008**, *47*, 2930-2946.

[17] Xin, S.; Guo, Y. G.; Wan, L. J. Nanocarbon networks for advanced rechargeable lithium batteries. *Acc. Chem. Res.* **2012**, *45*, 1759-1769.

[18] Armstrong, M. J.; O'Dwyer, C.; Macklin, W. J.; Holmes, J. D. Evaluating the performance of nanostructured materials as lithium-ion battery electrodes. *Nano Res.* **2014**, *7(1)*, 1-62.

[19] Bonaccorso, F.; Colombo, L.; Yu, G.; Stoller, M.; Tozzini, V.; Ferrari, A. C.; Ruoff, R. S.; Pellegrini, V. Graphene, related two-dimensional crystals, and hybird systems for energy conversion and storage. *Science* **2015**, *347*, 1246501-1.

[20] Yu, G.; Xie, X.; Pan, L.; Bao, Z.; Cui, Y. Hybrid nanostructured materials for high-performance electrochemical capacitors. *Nano Energy* **2013**, *2*, 213-234.

[21] Manthiram, A. Materials challenges and opportunities of lithium ion batteries. *J. Phys. Chem. Lett.* **2011**, *2*, 176-184.

[22] Zhu, H.; Jia, Z.; Chen, Y.; Weadock, N.; Wan, J.; Vaaland, O.; Han, X.; Li, T.; Hu, L. Tin anode for sodium-ion batteries using natural wood fiber as a mechanical buffer and electrolyte reservoir. *Nano Lett.* **2013**, *13*, 3093-3100.

[23] Lin, Y. M.; Abel, P. R.; Gupta, A.; Goodenough, J. B.; Heller, A.; Mullins, C. B.; Sn-Cu nanocomposite anodes for rechargeable sodium-ion batteries. *ACS Appl. Mater. Interfaces* **2013**, *5*, 8273-8277.

[24] Wu, Z. S.; Sun, Y.; Tan, Y. Z.; Yang, S.; Feng, X.; Mullen, K. Three-dimensional graphene-based macro- and mesoporous frameworks for high-performance electrochemical capacitive energy storage. *J. Am. Chem. Soc.* **2012**, *134*, 19532-19535.

[25] Chen, L. F.; Huang, Z. H.; Liang, H. W.; Cao, H. L.; Yu, S. H. Three-dimensional heteroatom-doped carbon nanofiber networks derived from bacterial cellulose for supercapacitors. *Adv. Func. Mater.* **2014**, *24*, 5104-5111.

[26] Song, H.; Yang, G.; Wang, C. General scalable strategy toward heterogeneously doped hierarchical porous graphitic carbon bubbles for lithium-ion battery anodes. *ACS Appl. Mater. Interfaces* **2014**, *6*, 21661–21668.

[27] Lyu, Z.; Xu, D.; Yang, L.; Che, R.; Feng, R.; Zhao, J.; Li, Y.; Wu, Q.; Wang, X.; Hu, Z. Hierarchical carbon nanocages confining high-loading sulfur for high-rate lithium-sulfur batteries. *Nano Energy* **2015**, *12*, 657-665.

[28] Tian, Y.; Hu, Z.; Yang, Y.; Wang, X.; Chen, X.; Xu, H.; Wu, Q.; Ji, W.; Chen, Y. In situ TA-MS study of the six-membered-ring-based growth of carbon nanotubes with benzene precursor. *J. Am. Chem. Soc.* **2004**, *126*, 1180-1183.

[29] Zhang, L.; Zhao, J.; Li, M.; Ni, H.; Zhang, J.; Feng, X.; Ma, Y.; Fan, Q.; Wang, X; Hu, Z; Huang, W. Preparation of graphene supported nickel nanoparticles and their application to methanol electrooxidation in alkaline medium. *New J. Chem.* **2012**, *36*, 1108-1113.

[30] Wu, Z. S.; Ren, W.; Xu, L.; Li, F.; Cheng, H. M. Doped graphene sheets as anode materials with superhigh rate and large capacity for lithium ion batteries. *ACS Nano* **2011**, *5*, 5463-5471.

[31] Fang, Y.; Lv, Y.; Che, R.; Wu, H.; Zhang, X.; Gu, D.; Zheng, G.; Zhao, D. Two-dimensional mesoporous carbon nanosheets and their derived graphene nanosheets: synthesis and efficient lithium ion storage. *J. Am. Chem. Soc.* **2013**, *135*, 1524-1530.

[32] Mukherjee, R.; Thomas, A. V.; Krishnamurthy, A.; Koratkar, N. Photothermally reduced graphene as high-power anodes for lithium-ion batteries. *ACS Nano* **2012**, *6*, 7867-7878.

[33] Xu, Y.; Lin, Z.; Zhong, X.; Papandrea, B.; Huang, Y.; Duan, X. Solvated graphene frameworks as high-performance anodes for lithium-ion batteries. *Angew. Chem. Int. Ed.* **2015**, *54*, 5345-5350.

[34] Liu, N.; Hu, L.; McDowell, M. T.; Jackson, A.; Cui, Y. Prelithiated silicon nanowires as an anode for lithium ion batteries. *ACS Nano* **2011**, *5*, 6487-6493.

[35] Volder, M. F. L. D.; Tawfick, S. H.; Baughman, R. H.; Hart, A. J. Carbon nanotubes: present and future commercial applications. *Science* **2013**, *339*, 535-539.

[36] Service, R. F. The next big(ger) thing. *Science* **2012**, *335*, 1167.

[37] Weiss, P. S. Mesoscale science: lessons from and opportunities for nanoscience." *ACS Nano* **2014**, *8*, 11025-11026.

[38] Lee, S. W.; Yabuuchi, N.; Gallant, B. M.; Chen, S.; Kim, B. S.; Hammond, P. T.; Yang, S. H. High-power lithium batteries from functionalized carbon-nanotube electrodes. *Nat. Nanotech.* **2010**, *5*, 531-537.

[39] Wu, Z. S.; Ren, W.; Xu, L.; Li, F.; Cheng, H. M. Doped graphene sheets as anode materials with superhigh rate and large capacity for lithium ion batteries. *ACS Nano* **2011**, *5*, 5463-5471.

[40] Wang, Z. L.; Xu, D.; Wang, H. G.; Wu, Z.; Zhang, X. B. In-situ fabrication of porous graphene electrodes for high-performance energy storage. *ACS Nano* **2013**, *7*, 2422-2430.

[41] Zhao, X.; Hayner, C. M.; Kung, M.; Kung, H. H. Flexible holey graphene paper electrodes with enhanced rate capability for energy storage applications. *ACS Nano* **2011**, *5*, 8739-8749.

[42] Kim, K. T.; Ai, G.; Chung, K. Y,; Yoon, C. S.; Yashiro, H.; Sun, Y. K.; Lu, J.; Amine, K.; Myung, S. T. Anatase titania nanorods as an intercalation anode material for rechargeable sodium batteries. *Nano Lett.* **2014**, *14*, 416-422.

[43] Cao, Y.; Xiao, L.; Sushko, M. L,; Wang, W.; Schwenzer, B.; Xiao, J.; Nie, Z.; Saraf, L. V.; Yang, Z.; Liu, J. Sodium ion insertion in hollow carbon nanowires for battery applications. *Nano Lett.* **2012**, *12*, 3783-3787.

[44] Tang, K.; Fu, L.; White, R. J.; Yu, L.; Titirici, M. M.; Antonietti, M.; Maier, J. Hollow carbon nanospheres with superior rate capability for sodium-based batteries. *Adv. Energy Mater.* **2012**, *2*, 873-877.

[45] Ding, J.; Wang, H.; Li, Z.; Kohandehghan, A.; Cui, K.; Xu, Z.; Zahiri, B.; Tan, X.; Lotfabad, E. M.; Olsen, B. C.; Mitlin, D. Carbon nanosheet frameworks derived from peat moss as high performance sodium ion battery anodes. *ACS Nano* **2013**, *7*, 11004-11015.

[46] Yan, Y.; Yin, Y. X.; Guo, Y. G.; Wan, L. J. A sandwich-like hierarchically porous carbon/graphene composite as a

high-performance anode material for sodium-ion batteries. *Adv. Energy Mater.* **2014**, DOI: 10.1002/aenm.201301584.

[47] Wen, Y.; He, K.; Zhu, Y.; Han, F.; Xu, Y.; Matsuda, I.; Ishii, Y.; Cumings, J.; Wang, C. Expanded graphite as superior anode for sodium-ion batteries, *Nat. Commun.* **2014**, *5*, 4033.

[48] Datta, D.; Li, J.; Shenoy, V. B. Defective graphene as a high-capacity anode material for Na- and Ca-ion batteries, *ACS Appl. Mater. Interfaces* **2014**, *6*, 1788-1795.

[49] Ghaffari, M.; Zhou, Y.; Xu, H.; Lin, M.; Kim, T.; Ruoff, R. S.; Zhang, Q. M. High-volumetric performance aligned nano-porous microwave exfoliated graphite oxide-based electrochemical capacitors. *Adv. Mater.* **2013**, *25*, 4879-4885.

[50] Yang, X.; Cheng, C.; Wang, Y.; Qiu, L.; Li, D. Liquid-mediated dense integration of graphene materials for compact capacitive energy storage. *Science* **2013**, *341*, 534-537.
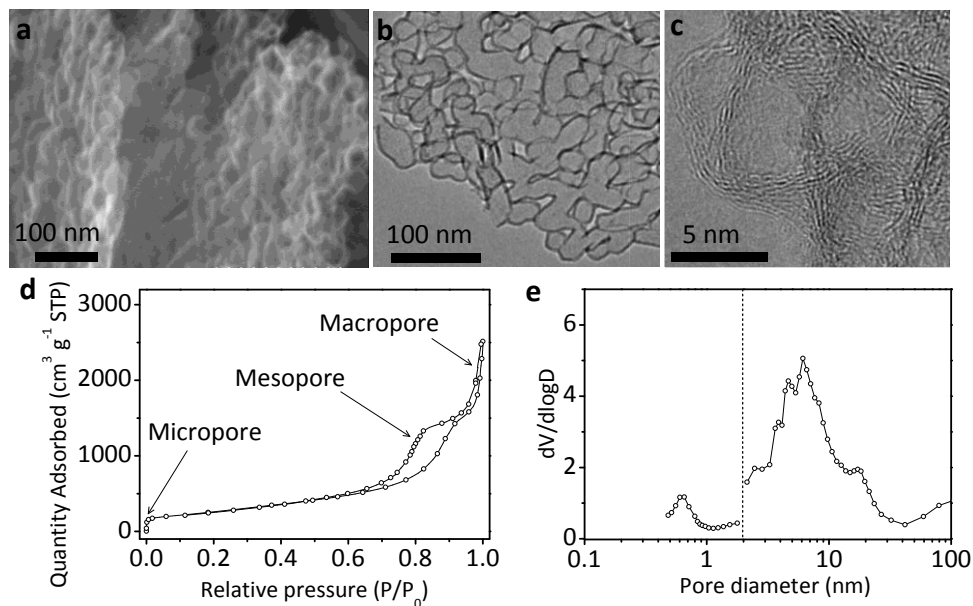
**Figure 1** Characterizations of the hCNC. (a) SEM image. (b) TEM image. (c) High resolution TEM image of the nanocages in (b) with well graphitic layers in shell. (d) $N_2$ adsorption and desorption isotherms, featured with the coexisting micro-, meso-, and macro-pores. (e) The corresponding micro-meso-macro pore size distributions.
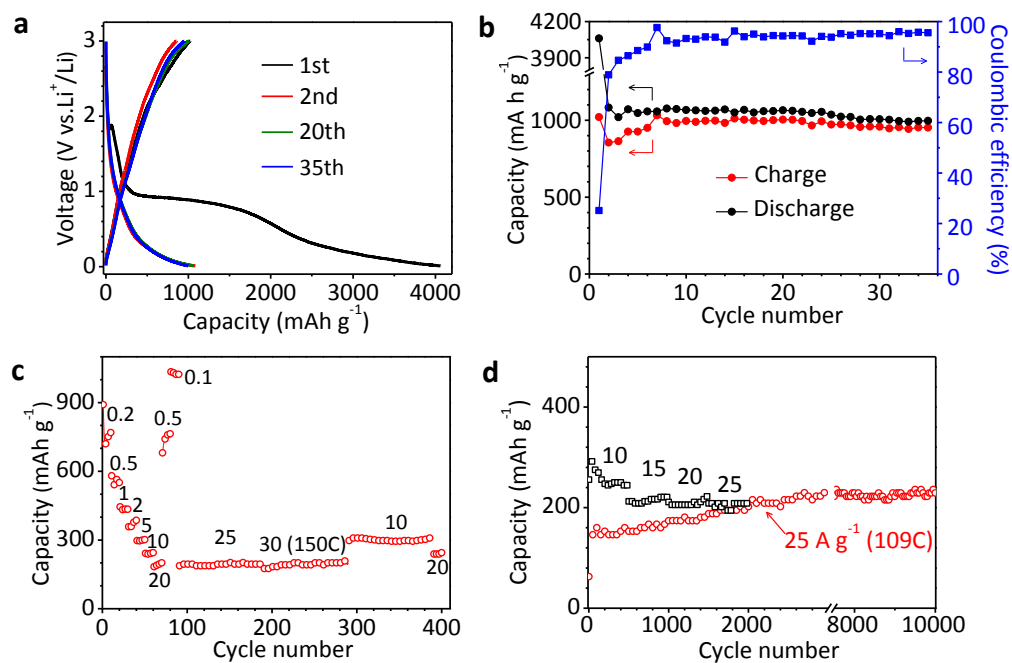


**Figure 2** Lithium storage performance of the hCNC. (a) Voltage profiles at a low current density of 0.1 A $g^{-1}$. (b) Cycle capability and Coulombic efficiency at the rate of 0.1 A $g^{-1}$. (c) Rate capability at different current densities (A $g^{-1}$). (d) High-rate capability at different current densities (A $g^{-1}$) (black line) and long-term cyclability at a current density of 25 A $g^{-1}$ for 10000 cycles (red line).
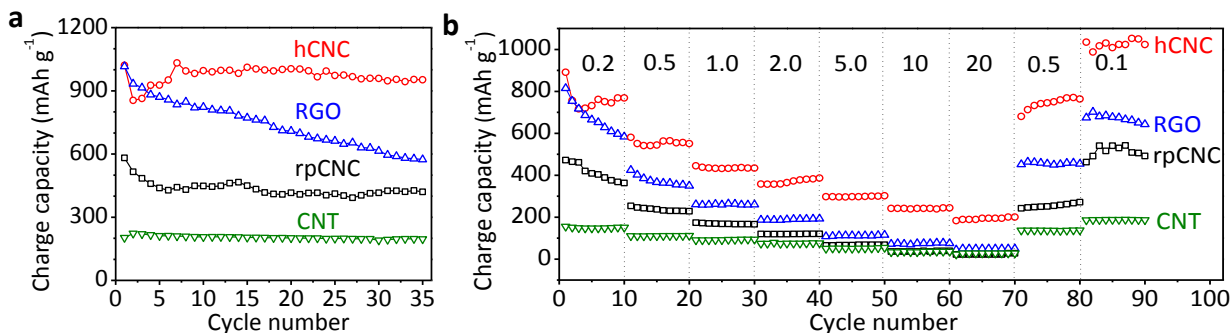
**Figure 3** Comparisons of the lithium storage performance for the four typical carbon nanomaterials of hCNC, rpCNC, CNT and RGO. (a) The reversible capacities at the rate of 0.1 A g$^{-1}$. (b) The rate performances at different current densities (A g$^{-1}$).
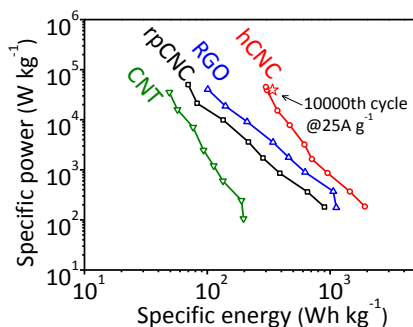


**Figure 4** Ragone plot for the hCNC based cell with lithium metal as the counter/reference electrode. The red pentagram represents the specific energy (339 Wh kg$_{electrode}$$^{-1}$) and specific power (37 kW kg$_{electrode}$$^{-1}$) for the hCNC after 10000 cycles at the current density of 25 A g$^{-1}$. (a) Comparison of Ragone plots for the hCNC and the rpCNC, CNT as well as RGO based cells.
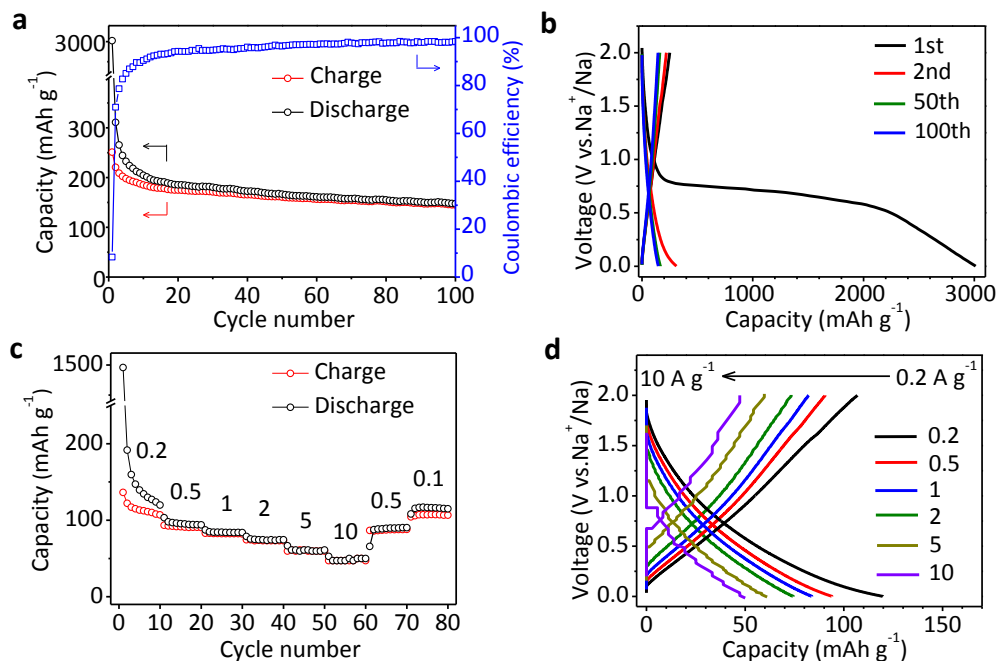


**Figure 5** Sodium storage performance of the hCNC. Cycle capability, Coulombic efficiency (a), and the corresponding voltage profiles (b) at a low rate of 0.1 A g$^{-1}$. The rate capability (c) and corresponding voltage profiles of the tenth cycle (d) at different rates (A g$^{-1}$).

# Electronic Supplementary Material

# Hierarchical carbon nanocages as high-rate anodes for Li- and Na-ion batteries

Zhiyang Lyu, Lijun Yang, Dan Xu, Jin Zhao, Hongwei Lai, Yufei Jiang, Qiang Wu, Yi Li, Xizhang Wang (✉), and Zheng Hu (✉)

*Key Laboratory of Mesoscopic Chemistry of MOE, School of Chemistry and Chemical Engineering, Nanjing University, Nanjing, 210093, China.*

**Table of Contents**

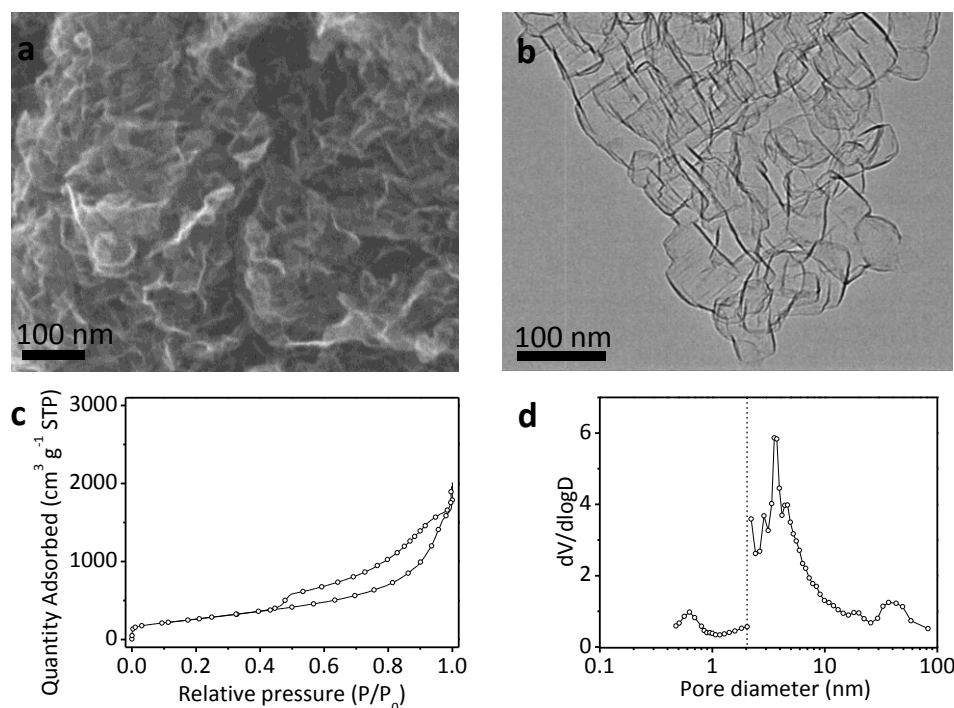Address correspondence to Xizhang Wang, wangxzh@nju.edu.cn; Zheng Hu, zhenghu@nju.edu.cn

**Figure S1** Characterizations of the rpCNC. (a) SEM image. (b) TEM image. (c) Nitrogen adsorption and desorption isotherms. (d) The corresponding pore size distributions.

From the SEM and TEM images (Figs. S1a and S1b and Fig. 1), the rpCNC and hCNC have the similar units of carbon nanocages at the nanoscale, but the quite different secondary structures at the mesoscale. The rpCNC has a large specific surface area of 997 $m^2$ $g^{-1}$ and a high micro-meso pore volume of 3.307 $cm^3$ $g^{-1}$ (Figs. S1c and S1d), which are close to the values of hCNC.
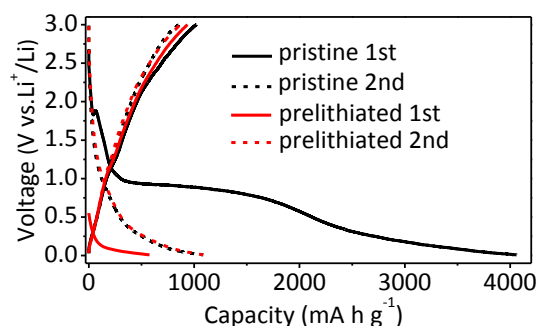


**Figure S2** Electrochemical performance of the prelithiated hCNC electrode. The voltage profiles of the initial two cycles for the hCNC before and after prelithiation were performed at the current density of 0.1 A $g^{-1}$.

The prelithiation experimental was done as follow: the hCNC electrode infiltrated by the electrolyte was directly attached to a piece of Li foil for 3 h[S1,S2]. After that, the electrochemical performance of the prelithiated hCNC electrode was evaluated with the same procedure as that for the pristine hCNC. The open circuit voltage of the cell with the prelithiated hCNC is 0.55 V, which is much lower than that of the pristine hCNC (2.65 V), since the Li insertion reduces the potential of the hCNC versus Li foil.

For the pristine hCNC, the first discharge and charge capacities are 4061 and 1021 mAh $g^{-1}$ with a large irreversible capacity of 3040 mAh $g^{-1}$. As a comparison, for the prelithiated hCNC, the first discharge and charge capacities are 576 and 932 mAh $g^{-1}$ without irreversible capacity. This indicates that the prelithiation could effectively avoid the large irreversible capacity due to the formation SEI layer in advance.
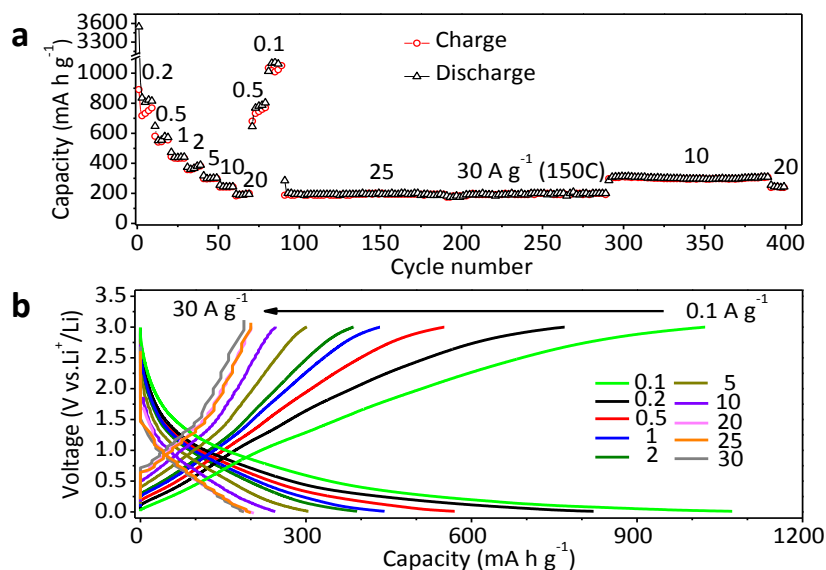
**Figure S3** Rate performance of the hCNC electrodes for Li storage. a, The rate performance at different current densities (A g$^{-1}$). b, The corresponding voltage profiles of the last cycles at different current densities.

It is observed that there are some abnormal serrated characteristics for the charge-discharge curves at very high current densities, e.g., at 25 and 30 A g$^{-1}$, in Figure S3b. At such high current densities, the specific capacities are very small. As a result, the record data are sparse, which leads to the serrated characteristics.
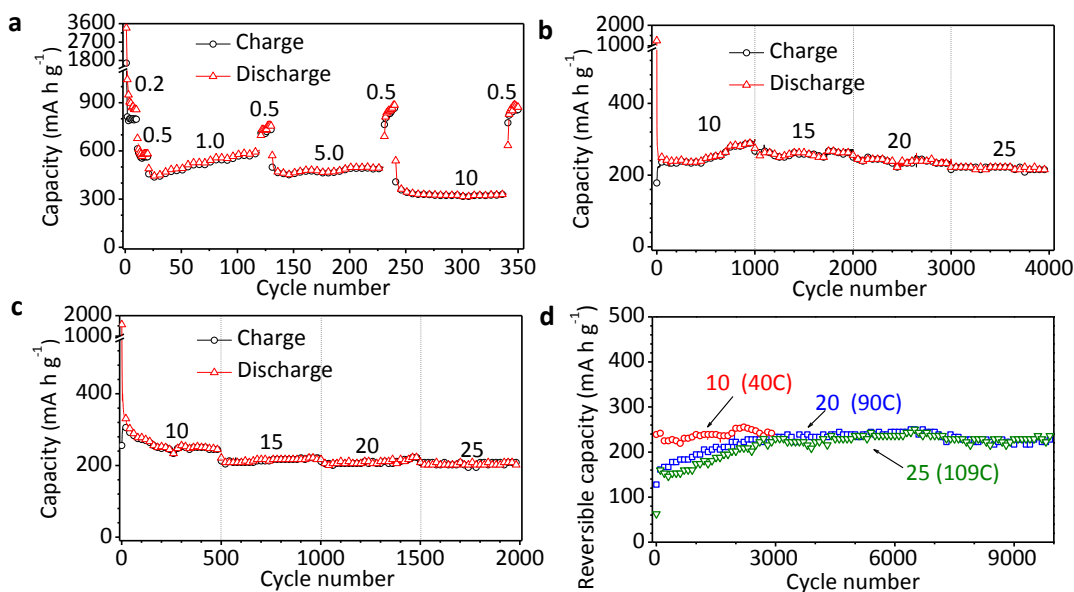


**Figure S4** High-rate performances and long-term cycle abilities of hCNC electrodes for Li storage. a-c, High-rate performances of three typical hCNC electrodes at different current densities (A g$^{-1}$).  d, Long-term cycle abilities of the hCNC electrodes at a current density of 10 A g$^{-1}$ for 3000 cycles, 20 and 25 A g$^{-1}$ for 10000 cycles.

The capacities of the hCNC electrodes at the same current density may somewhat different from cell to cell, but fluctuates at the same level of high-rate capability and long-term cycle abilities.
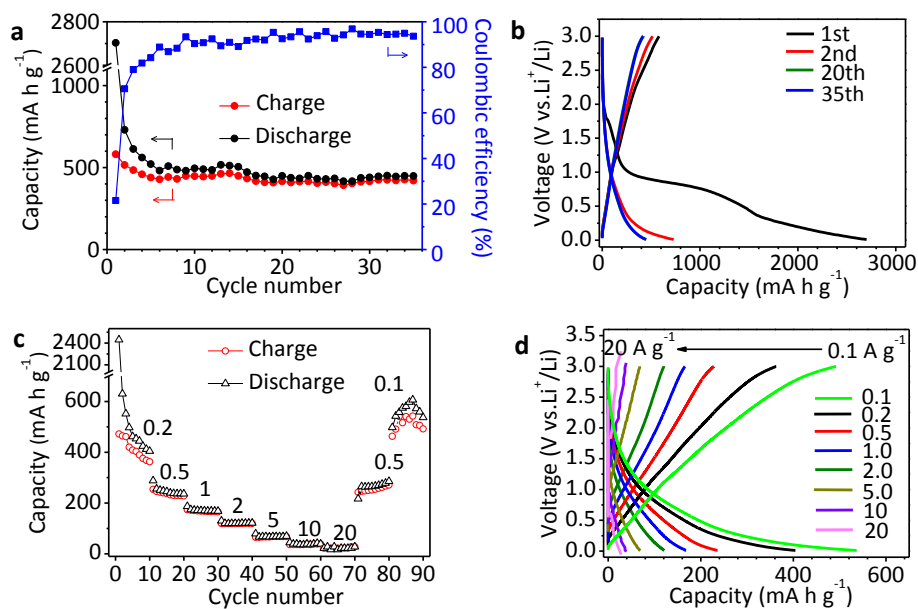
**Figure S5** Li storage performance of the rpCNC electrodes. a,b, Cycle capability and Coulombic efficiency, and the corresponding voltage profiles at a low current density of 0.1 A g$^{-1}$. c,d, The rate performance and corresponding voltage profiles of the tenth cycle at different current densities (A g$^{-1}$).



**Figure S6** Li storage performance of the CNT electrodes. a,b, Cycle capability and Coulombic efficiency, and the corresponding voltage profiles at a low current density of 0.1 A g$^{-1}$. c,d, The rate performance and corresponding voltage profiles of the tenth cycle at different current densities (A g$^{-1}$).
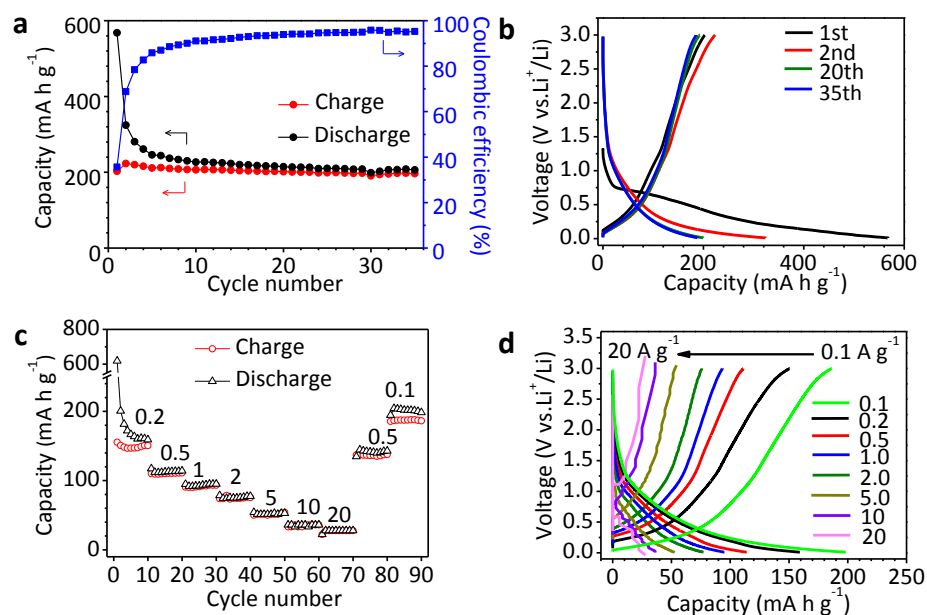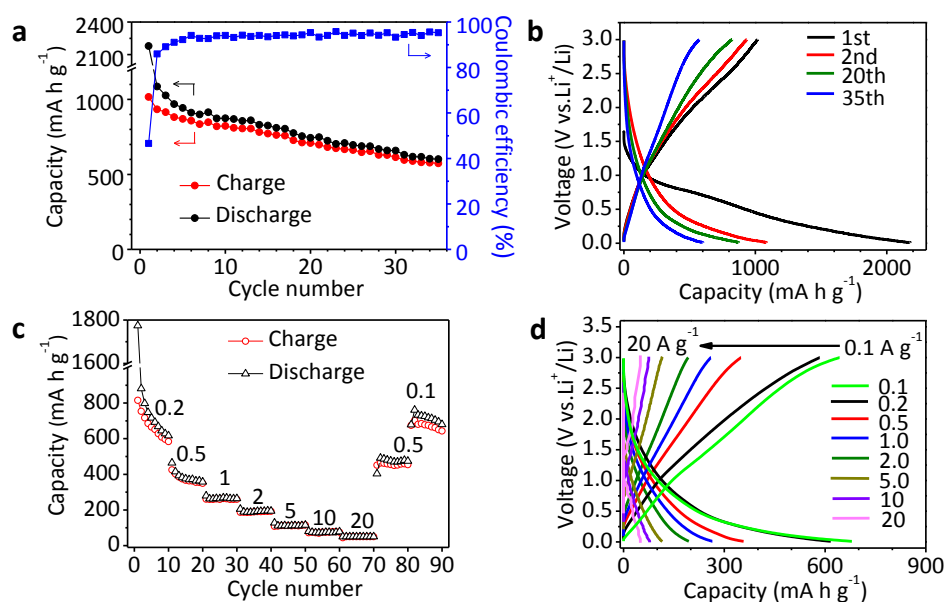
**Figure S7** Li storage performance of the RGO electrodes. a,b, Cycle capability and Coulombic efficiency, and the corresponding voltage profiles at a low current density of 0.1 A g$^{-1}$. c,d, The rate performance and corresponding voltage profiles of the tenth cycle at different current densities (A g$^{-1}$).

The capacity fades rapidly in the first few cycles and stabilizes at a lower stage. In the first cycle, a reversible charge capacity of 1016 mAh g$^{-1}$ is achieved; but after 35 cycles, the reversible charge capacity drops to 574 mAh g$^{-1}$, with a large capacity loss of 43.5%. The poor cyclability of RGO electrode should be induced by the inter-sheet aggregation[S3].
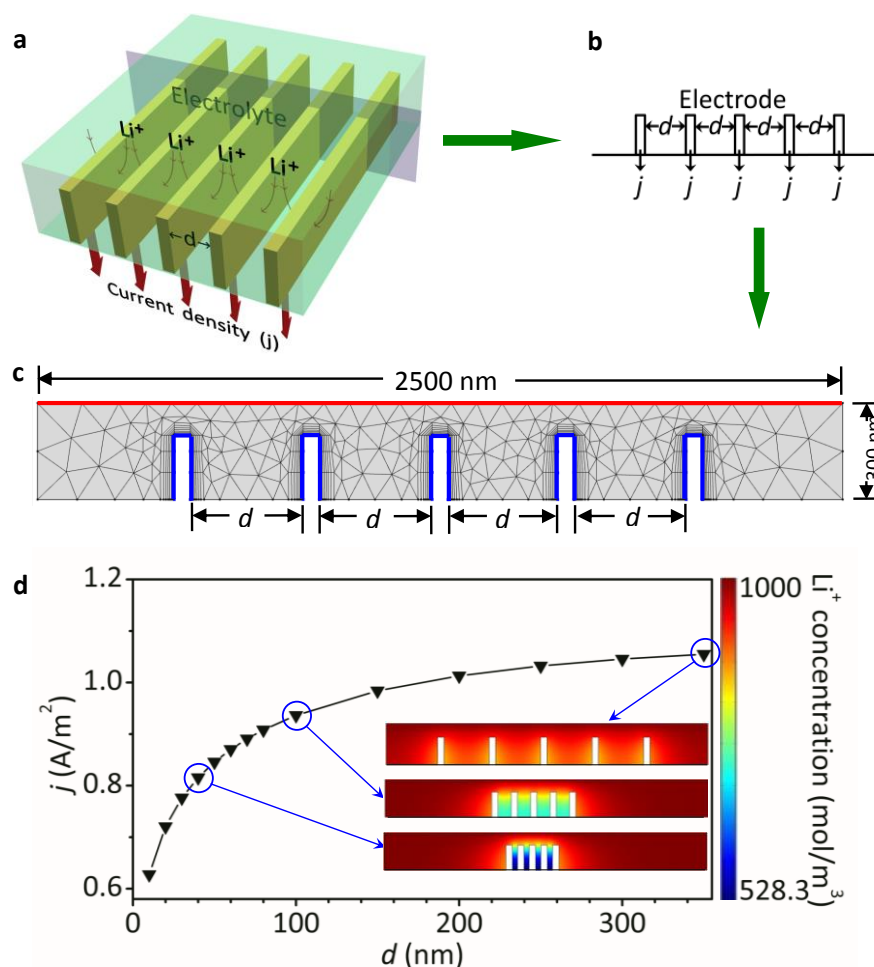
**Figure S8** A half-cell model with a 3D electrode and corresponding simulation results. a, The 3D model consisting of five parallel sheets with inter-sheet space (d). b, The cross-sectional 2D model. c,d, The finite element method (FEM) model (c) and corresponding simulation results (d). For a specific d, the balance between Li ions supply and consumption reaches the steady-state electrode reaction current density (j) which is an indicator of the rate of Li storage. The colored inset in (d) figures the steady Li ion concentrations.

To understand the superiority of the 3D hierarchical architecture, we performed the theoretical simulation by using the finite element method (FEM).[S4] First, a simple half-cell model with a 3D electrode has been built which consists of five parallel sheets soaked in the electrolyte (Fig. S8a). Due to symmetry along the height, the 3D geometry can be modeled using a 2D cross section (Fig. S8b).[S5] The corresponding FEM model takes the size of 2500 nm $\times$ 300 nm (Fig. S8c). Five blocks with 50 nm $\times$ 200 nm in size for each and interspace $d$ are surrounded by the electrolyte. The electrolyte (gray area) is based on the solvent mixture [1:2 (v/v) EC and DMC] and the $LiPF_6$ salt with the initial concentration of 1000 mol m$^{-3}$. The electrolyte salt diffusion coefficient is set to be $7.5 \times 10^{-11}$ m$^2$ s$^{-1}$ (ref. S6). During simulation, the concentration is fixed at 1000 mol m$^{-3}$ and the potential at 1.05 V for the upper boundary (red line in Fig. S8c). The coupled Li ion diffusion and insertion processes of the model electrodes were simulated. The full set of Butler-Volmer electrode kinetics and Fickian diffusion equations were solved in the steady-state regime. Thus, the obtained steady state reaction current density ($j$) is directly associated with the electrode microstructure (Fig. S8d). Specifically:

$j$ increases with increasing $d$, accompanied by the increasing Li ion concentration around the electrode sheets (inset in Fig. S8d). This changing behavior is particularly intensive in the small $d$ side (e.g. $d<50$ nm) and gradually gets mild in the large $d$ side (e.g. $d>50$ nm). This is reasonable since the narrow inter-sheet space would hinder the transportation of Li ion, leading to a low Li ion concentration around the electrode, thereby a low electrode reaction current. On the contrary, the wide inter-sheet space could well facilitate the transportation of Li ion around the

electrode, thus maintaining a high Li ion concentration, thereby a high electrode reaction current. This simulation result supports the much better performance of the hierarchical hCNC electrode with a submicron-sized inter-sheet space than that of the closely packed rpCNC electrode with a narrow interspace.

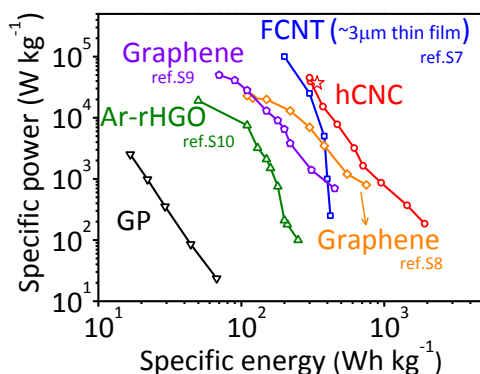**Note:** EC: ethylene carbonate; DMC: dimethyl carbonate.



**Figure S9** Ragone plots of the hCNC and the updated pure carbon materials based half cells for comparison.

Four Ragone plots of the half cells for the state-of-the-art pure carbon materials of FCNT[S7], graphene[S8,S9] and Ar-rHGO[S10] are taken from recent literatures. The Ragone plots of the half cells for the hCNC and commercial graphite powder (GP) in this study are also presented here. It is seen that the plot of the hCNC locates in the most upper-right side, indicating the superb performance. The upmost point of the hCNC reaches a high specific power of 45 kW $kg_{electrode}^{-1}$ and a high specific energy of 300 Wh $kg_{electrode}^{-1}$ under the high charging current density of 30 A $g^{-1}$ (150C, 24 s for full-charging).

**Note:**
1) Although the plot of the FCNT has the highest specific power within a certain narrow specific energy range (see the upmost point), the thickness of the electrode in that study is only ~3 μm, much thinner than that of the conventional electrodes. The hCNC electrodes in this study have the thickness of about 25~55 μm (Fig. S12), close to the practical requirements.
2) FCNT: functionalized carbon naontubes[S7]
3) Graphene: (refs S8, S9)
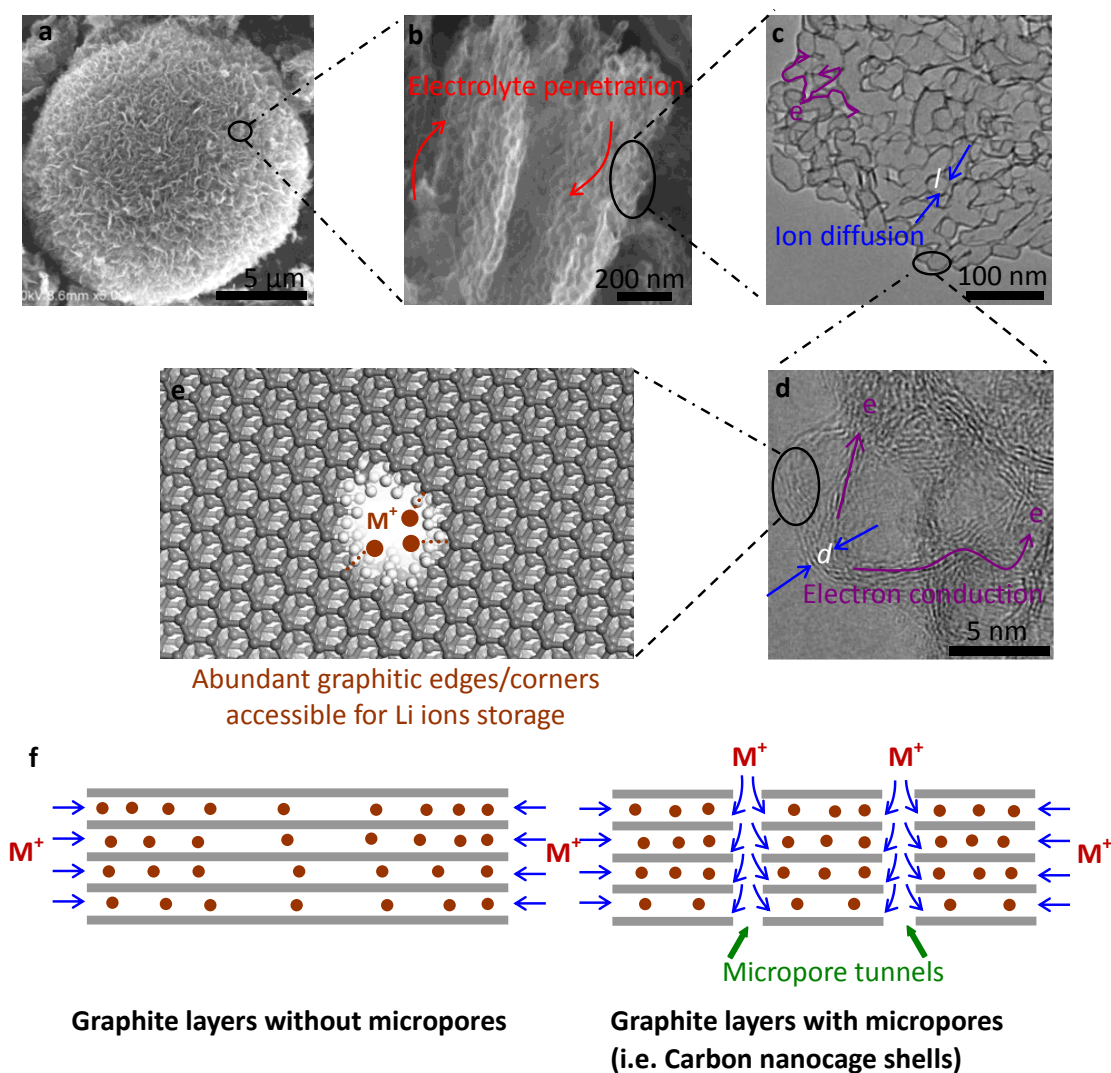4) Ar-rHGO: Ar-reduced holey graphene oxides[S10]

**Figure S10** A schematic diagram of electrolyte penetration, ion diffusion and electron conduction for the high-rate performance of the hCNC. In **e** and **f**, M$^+$ stands for Li$^+$ or Na$^+$.

As described in our previous paper[S11], the hCNC product owns a 3D hierarchical architecture with well-defined multiscale characters. The micron-sized sphere-like carbon particles are composed of the nanosheets with submicron-sized interspace, while the nanosheets consist of the interconnected cuboidal hollow nanocages. Specifically:

(**a**) micron-sized dimensions of the sphere-like carbon particles;

(**b**) submicron-sized interspace between the neighboring thin nanosheets;

(**c**) 10~50 nm sizes of the inter-connected hollow nanocages (small *l*);

(**d**) 4~7 graphitic layers of the shell thickness (small *d*).

(**e**,**f**) micropore tunnels through the graphite shells (~0.6 nm).

First, the electrolyte can rapidly soak the hCNC electrode over each nanocage due to the large inter-sheet space (Fig. S10b), thin thickness of each sheet (Fig. S10b), the mesoporous network, as well as the unsealed shells (Fig. S10c,e).

Second, the solid-state Li or Na ion diffusion length is short enough for rapid ion transport since the nanocages are rather small with thin shells (i.e. *l* and *d* are small enough), with the abundant micropore tunnels of the unsealed shells (Fig. S10c-f). As schemed in Fig. S10f, the solid-state ion diffusion in the graphite layers with micropores (right) is much easier than that in the graphite layers without micropores (left). Thus the Li or Na ions can rapidly

transport across the active sites.

Third, good electron conductivity can be expected due to the interconnection or sharing the carbon shells between the neighboring nanocages (Fig. S10c,d).

Fourth, more active sites for Li or Na storage are available due to the existence of micropore tunnels which allows the inner surface accessible for Li or Na ions, and provides abundant graphitic edges/corners[S12] (Fig. S10e and Fig. S11).

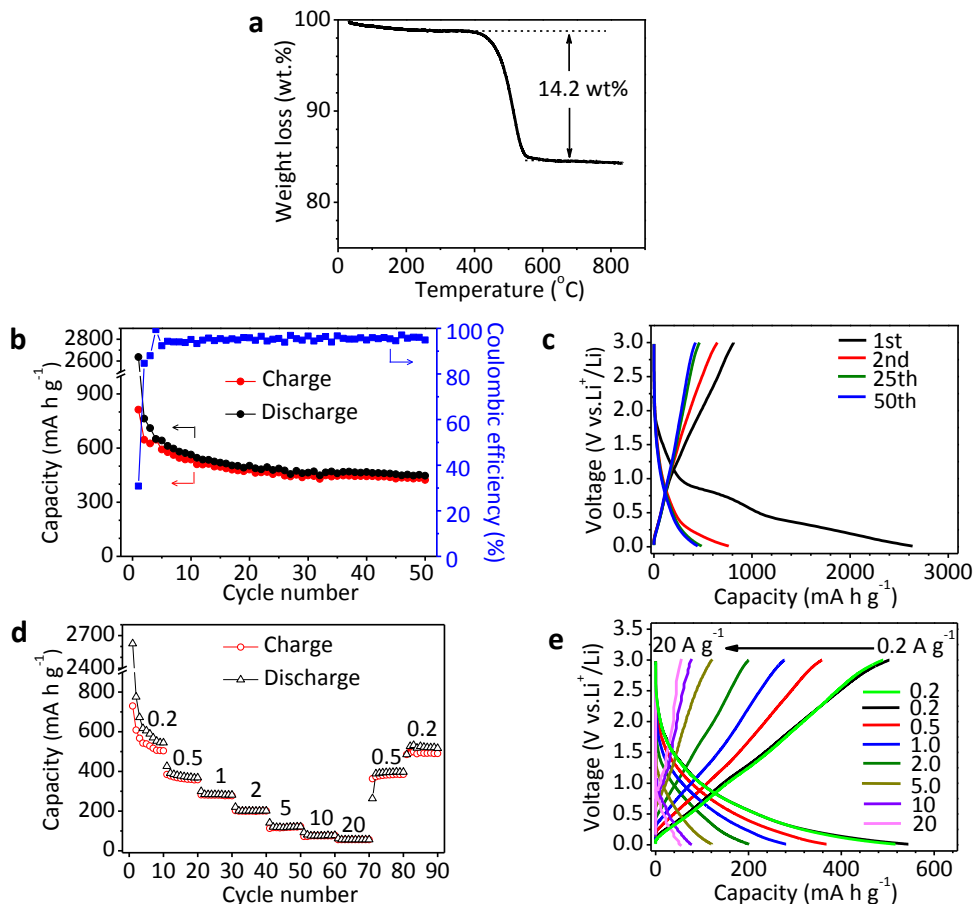The above four points make the main contribution to the high-rate performance of the hCNC electrodes.



**Figure S11** Thermogravimetry curve and Li storage performance of the MgO@hCNC intermediate product. a, Thermogravimetry curve. b,c, Cycle capability and Coulombic efficiency, and the corresponding voltage profiles at a low current density of 0.1 A g$^{-1}$ (the mass is based on carbon). d,e, The rate performance and corresponding voltage profiles of the tenth cycle at different current densities (A g$^{-1}$).

Thermogravimetry analysis indicates the MgO@hCNC has the carbon content of ca. 14.2 wt% (Fig. S11a). In the first cycle, its reversible charge capacity is 813 mAh g$^{-1}$ (the mass is based on carbon). After 50 cycles the capacity drops to 424 mAh g$^{-1}$ (Fig. S11b,c), only about half of that for the hCNC at the same condition (Fig. 2). This result manifests that the removal of the inside MgO template could release the large inner surface for lithium storage. The rate performance (Fig. S11d,e) is also not as good as that of the hCNC (Fig. 2), indicates the contribution of the inner surface of the hCNC.
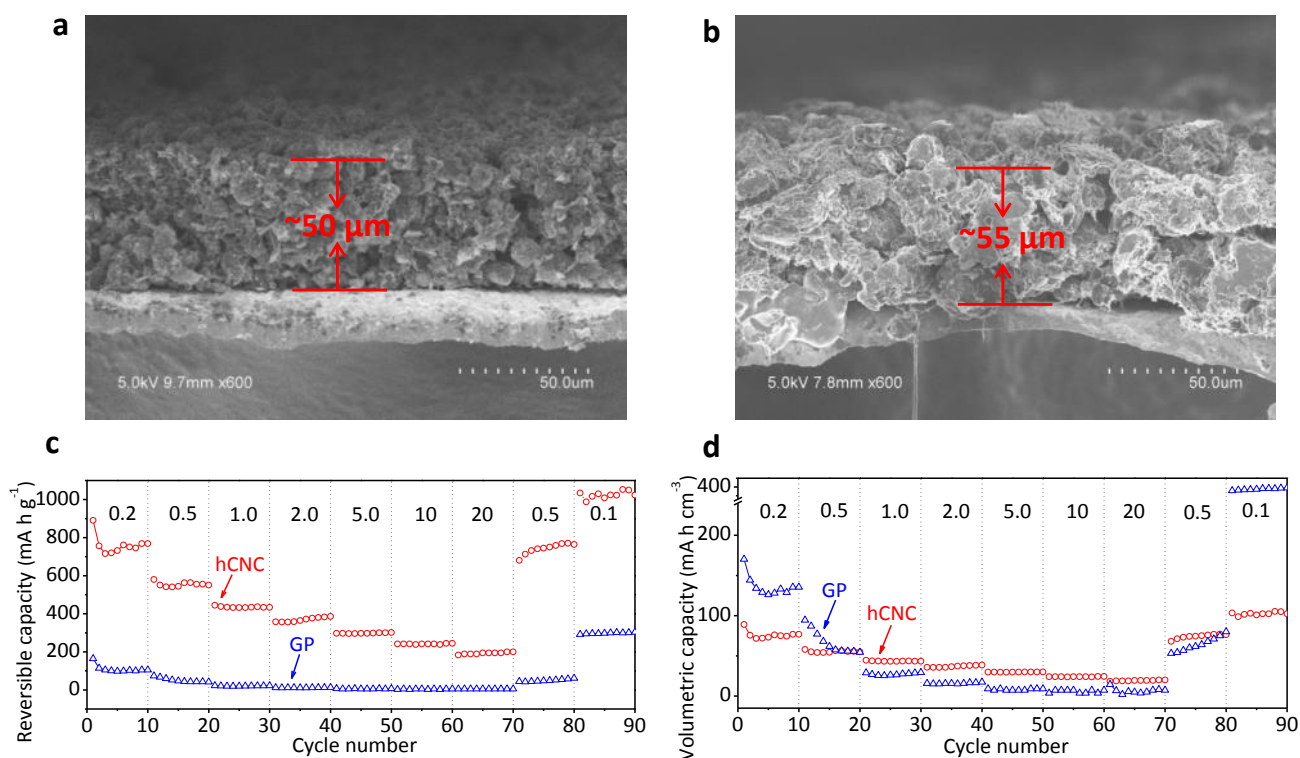
**Figure S12** SEM images and rate performance comparison for Li storage of the hCNC and GP electrodes. a,b, SEM image of the hCNC electrode and GP electrode, respectively. c,d, Rate performance comparison between the hCNC and GP electrodes in specific capacity and volumetric capacity, respectively.

In Fig. S12a,b, with the loading of ~0.5 mg cm$^{-2}$ and ~7.0 mg cm$^{-2}$ for hCNC and GP, the corresponding electrode has the thickness of about 50 μm and 55 μm, giving the tap density ($d$) of about 0.1 and 1.3 g cm$^{-3}$, respectively.

As known, in addition to the specific capacity ($C$), the volumetric capacity ($V$) is also an important parameter for practical applications. Specifically, $V = C \times d$.

Thus, the rate performance comparison between the GP and hCNC electrodes in terms of $C$ in Fig. S12c is converted in terms of $V$ as shown in Fig. S12d. The volumetric capacity of hCNC electrode is clearly higher than that of GP electrode at high current densities.

For ultrahigh rate application, the state-of-the-art cathode materials have reached the half-cell capacity up to ~120 mAh g$^{-1}$ at 200C rate[S13]. In our case, the hCNC anode electrode possesses the high steady capacity up to ~190 mAh g$^{-1}$ at 150C rate as well as the superb volumetric capacity. Therefore, our multiscale hierarchical carbon nanocage provides an ideal anode candidate for the high-rate LIBs.
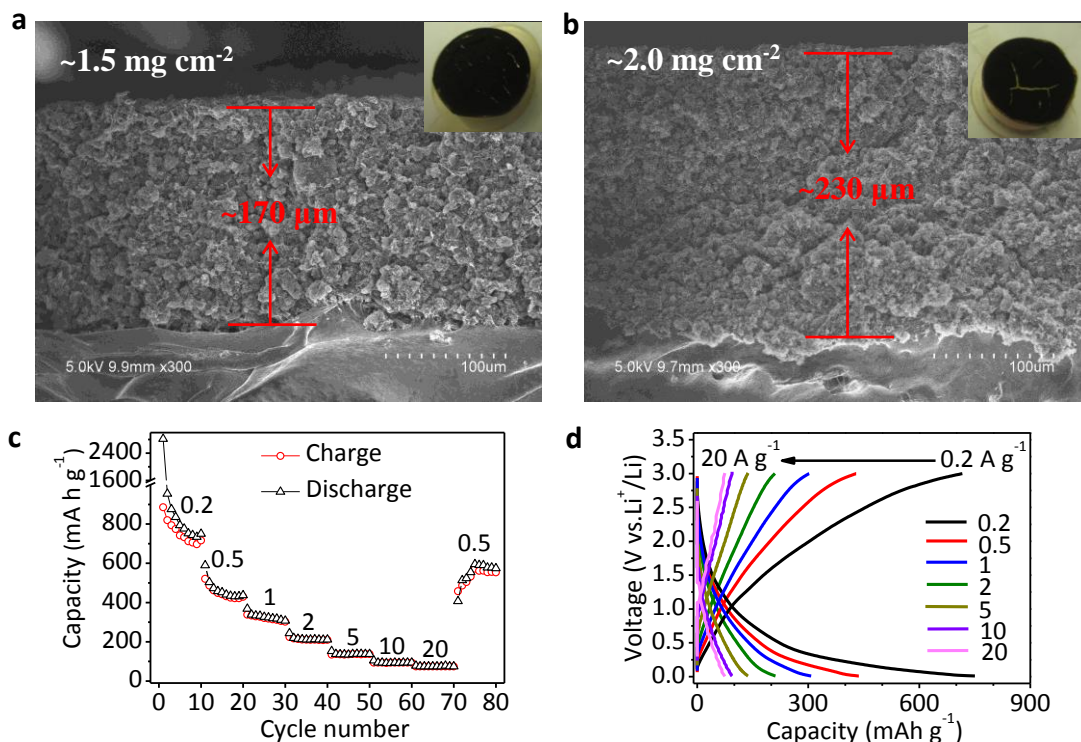
**Figure S13** SEM images and electrochemical performance for the high mass loading of hCNC electrodes. a,b, SEM images of the hCNC electrodes with ~1.5 and ~2.0 mg cm$^{-2}$, respectively. Insets are the photographs of the hCNC electrode films. c,d, The rate performance and corresponding voltage profiles of the tenth cycle at different current densities (A g$^{-1}$) for the hCNC electrodes with ~1.5 mg cm$^{-2}$ mass loading.

To investigate the effect of the mass loading of electrodes on the rate performance, the mass loadings of electrodes are intentionally increased to 1.0~2.0 mg cm$^{-2}$. The thickness of the electrode films increased correspondingly, e.g., ~170 and 230 μm for 1.5 and 2.0 mg cm$^{-2}$ (Figure S13a and S13b), obviously thicker than ~50 μm for 0.5 mg cm$^{-2}$ (close to the practical requirements) (Figure S12a). Noticeably, the films easily peeled off the substrates. Their electrochemical measurements were carried out. The rate performances of the hCNC electrode with ~1.5 mg cm$^{-2}$ are shown in Figure S13c and S13d, which is not so good as that of the electrode with low mass loading (0.25~0.5 mg cm$^{-2}$) (Figure 2). This could be attributed to the sluggish ion and electron transportations in the thick and cracked films. With further increasing the thickness of electrode, the rate performance becomes even worse. Similar phenomenon happened to the functionalized carbon nanotubes [S7].

## References

S1 Hassoun, J.; Lee, K. S.; Sun, Y. K.; Scrosati, B. An advanced lithium ion battery based on high performance electrode materials. *J. Am. Chem. Soc.* **2011**, *133*, 3139-3143.

S2 Liu, N.; Hu, L.; McDowell, M. T.; Jackson, A.; Cui, Y. Prelithiated silicon nanowires as an anode for lithium ion batteries. *ACS Nano* **2011**, *5*, 6487-6493.

S3 Li, D.; Kaner, R. B. Graphene-based materials. *Science* **2008**, *320*, 1170-1171.

S4 Comsol Group, COMSOL Multiphysics, COMSOL, Ab., (online) Available at: http://www.comsol.com/.

S5 http://www.comsol.com/showroom/gallery/9981/.

S6 Doyle, M., Newman, J., Gozdz, A. S., Schmutz, C. N. & Tarascon, J. M. Comparison of modeling predictions with experimental data from plastic lithium ion cells. *J. Electrochem. Soc.* **1996**, *143*, 1890-1903.

S7 Lee, S. W.; Yabuuchi, N.; Gallant, B. M.; Chen, S.; Kim, B. S.; Hammond, P. T.; Yang, S. H. High-power lithium batteries from functionalized carbon-nanotube electrodes. *Nat. Nanotech.* **2010**, *5*, 531-537.

S8 Wu, Z. S.; Ren, W.; Xu, L.; Li, F.; Cheng, H. M. Doped graphene sheets as anode materials with superhigh rate and large capacity for lithium ion batteries. *ACS Nano* **2011**, *5*, 5463-5471.

S9 Wang, Z. L.; Xu, D.; Wang, H. G.; Wu, Z.; Zhang, X. B. In-situ fabrication of porous graphene electrodes for high-performance energy storage. *ACS Nano* **2013**, *7*, 2422-2430.

S10 Zhao, X.; Hayner, C. M.; Kung, M.; Kung, H. H. Flexible holey graphene paper electrodes with enhanced rate capability for energy storage applications. *ACS Nano* **2011**, *5*, 8739-8749.

S11 Lyu, Z.; Xu, D.; Yang, L.; Che, R.; Feng, R.; Zhao, J.; Li, Y.; Wu, Q.; Wang, X.; Hu, Z. Hierarchical carbon nanocages confining high-loading sulfur for high-rate lithium-sulfur batteries. *Nano Energy* **2015**, *12*, 657-665.

S12 Kaskhedikar, N. A.; Joachim, M. Lithium storage in carbon nanostructures. *Adv. Mater.* **2009**, *21*, 2664-2680.

S13 Kang, B.; Ceder, G. Battery materials for ultrafast charging and discharging. *Nature* **2009**, *458*, 190-193.